Update of the Seismogenic Potential of the Upper Rhine Graben Southern Region

Sylvain Michel[1,2], Clara Duverger[2], Laurent Bollinger[2], Jorge Jara[1], Romain Jolivet[1,3]

[1] Laboratoire de Géologie, Département de Géosciences, Ecole Normale Supérieure, PSL Université, CNRS UMR 8538, 24 Rue Lhomond, 75005, Paris, France.
[2] CEA, DAM, DIF, F-91297 Arpajon, France
[3] Institut Universitaire de France, 1 rue Descartes, 75005, Paris

Correspondence to: Sylvain Michel (sylvain_michel@live.fr)

Abstract.

The Upper Rhine Graben (URG), located in France and Germany, is bordered by north-south trending faults, some of which are considered active, posing a potential threat to the dense population and infrastructures on the Alsace plain. The largest historical earthquake in the region was the M6.5+/-0.5 Basel earthquake in 1356. Current seismicity (M>2.5 since 1960) is mostly diffuse and located within the graben. We build upon previous seismic hazard studies of the URG by exploring uncertainties in greater detail and revisiting a number of assumptions. We first take into account the limited evidence of neotectonic activity, then explore tectonic scenarios that have not been taken into account previously, exploring uncertainties for M_{max}, its recurrence time, the *b*-value, and the moment released aseismically or through aftershocks. Uncertainties on faults' moment deficit rates, on the observed seismic events' magnitude-frequency distribution, and on the moment-area scaling law of earthquakes are also explored. Assuming a purely dip-slip / normal faulting mechanism associated to a simplified 3 main fault model, M_{max} maximum probability is estimated at $M_w6.1$. Considering this scenario, there would be a 99% probability that M_{max} is less than 7.3. In contrast, with a strike slip assumption associated to a 4 main fault model, consistent with recent paleoseismological studies and the present-day stress field, M_{max} is estimated at $M_w6.8$. Based on this scenario, there would be a 99% probability that M_{max} is less than 7.6.

1 INTRODUCTION

The Upper Rhine Graben (URG), located in France and Germany, is bounded by north-south trending faults, some of which are considered active, posing a potential threat to the dense population and the industrial and communication infrastructures of the Alsace plain (Figure 1). The largest historical earthquake in the region was the 1356 Basel earthquake with a maximum intensity equal to or greater than IX (Mayer-Rosa and Cadiot, 1979; Fäh et al., 2009), an earthquake presently associated to a magnitude between M6.5+/-0.5 (Manchuel et al., 2017) and M6.9+/-0.2 (Fäh et al., 2009). Current seismicity (M>2.5 since 1960) is mostly diffuse and located within the graben (Doubre et al., 2022), hence the difficulty to attribute individual events to a given fault segment. The bordering faults themselves are relatively quiet except for the south-eastern section of the graben, near Mulhouse-Basel, where natural seismic sequences (ROULAND et al., 1983; Bonjer, 1997) and induced seismicity (Kraft and Deichmann, 2014) have been observed. Seismic activity actually varies along the URG with an increasing rate of events towards the south (Barth et al., 2015). The relative rate between small and large events (b-value from the Gutenberg-Richter law) also increases towards the south indicating a surplus of small earthquakes or a deficit of large events roughly south of Strasbourg (Barth et al., 2015). Focal mechanisms of earthquakes suggest that the region is subject to strike-slip regime with some normal component (Mazzotti et al., 2021), consistent with the large wavelength strain inferred from geodetic data (Henrion et al., 2020). Characterizing the slip rates of the graben's faults based on geodetic data remains challenging. Indeed regional glacial isostatic adjustments, local subsidence and low tectonic strain rates result in a heterogeneous velocity field with values below 0.2 mm/yr and often within measurement uncertainties (Fuhrmann et al., 2015; Henrion et al., 2020).

The seismic hazard of the URG has been evaluated by multiple studies at the national/European scale (Grünthal et al., 2018; Drouet et al., 2020; Danciu et al., 2021). Furthermore, the seismic hazard of the southern region of the URG in particular has recently been assessed by Chartier et al. (2017) with a focus on the Fessenheim nuclear power plant (Figure 1). This study evaluates the seismic hazard using a fault-based approach, taking into account the network of potentially active faults characterized by Jomard et al. (2017). This fault-based work involves a moment budget approach, which involves comparing the rate of moment release by seismicity and the rate of moment deficit (MDR) accumulating along locked portions of faults between large earthquakes (i.e. the tectonic loading rate of each fault). Since the period of seismological observation (a few centuries) is too short to be representative of the long-term behavior of seismicity, Chartier et al. (2017) built instead a seismicity model assumed to be representative of the long-term Magnitude-Frequency Distribution (MFD) of earthquakes, a method similarly used in former studies (e.g. Molnar, 1979; Anderson and Luco, 1983; Avouac, 2015). Earthquakes below

58   M_w5 are disregarded (Bommer and Crowley, 2017; Chartier et al., 2017). Earthquakes between M_w5 and 6 are

59   assumed to follow the MFD of the catalog of earthquakes they consider. This catalog integrates several sources of

60   instrumental and historical earthquakes including sources from the *Laboratoire de Détection et de Géophysique*

61   of the *Commissariat à l'Énergie Atomique et aux énergies alternatives* (CEA-LDG; http://www-dase.cea.fr/) and

62   from the FPEC (French Parametric Earthquake Catalogue; Baumont and Scotti, 2011), the IRSN contribution to

63   SHEEC (SHARE European Earthquake Catalogue; Stucchi et al., 2013). MFDs are estimated based on a French

64   seismotectonic zoning scheme defined by Baize et al. (2013). Earthquakes with magnitude above M_w6 are assumed

65   to occur on the fault planes (Jomard et al., 2017). Chartier et al. (2017) consider two types of model: (1) Each fault

66   ruptures only as its maximum magnitude event, which is controlled by the surface area of the seismogenic fault

67   segment (characteristic earthquake model); (2) Events follow the Gutenberg-Richter (GR) law with a b-value equal

68   to 1, and the maximum magnitude, M_{max}, is fixed as in the previous model. The recurrence times of the $M_w>6$

69   events are then calibrated so that the rate of moment released by the seismicity models matches the MDR estimated

70   from neotectonic data (Chartier et al., 2017; Jomard et al., 2017). The authors explore different fault geometries

71   (e.g. dip and seismogenic depth) using a logic-tree methodology and then proceed to the Probabilistic Seismic

72   Hazard Assessment (PSHA) of the region, providing a map of the probability of exceedance of Peak Ground

73   Acceleration (PGA) within a time period.

74   A number of strong assumptions are made within this framework. As mentioned previously, a simplified fault

75   network is used (Jomard et al., 2017), which constrains the seismogenic area available for ruptures. Expert choices

76   have also been made to distribute slip rates (i.e. loading rates) originally attributed to faults that have been removed

77   from the initial fault network (Nivière et al., 2008) on other fault segments. On a number of faults, no estimates of

78   neotectonic slip rate are available (e.g. West Rhenish Fault) and the authors have chosen to apply slip rates

79   equivalent to those from other nearby faults (0.01 to 0.05 mm/yr). The neotectonic data are actually only along-

80   dip slip rate estimates. No along-strike slip rates have yet been published due to the lack of markers to quantify

81   horizontal offsets along faults and this component has thus been ignored. In addition, Chartier et al. (2017) do not

82   consider continuous probabilities as they apply a logic-tree method. Chartier et al (2017) fix the b-value to 1,

83   choose the seismogenic depth to be either 15 or 20 km and do not take into account multi-segment ruptures when

84   estimating a M_{max} for each fault segment.

85   In this study, we build upon Chartier et al. (2017) seismic hazard evaluation of the southern URG by exploring

86   uncertainties in greater detail, revisiting a number of assumptions. We use the methodology from Rollins and

87   Avouac (2019) and Michel et al. (2021), which allows to evaluate the seismogenic potential of faults in a

88   probabilistic fashion and explore uncertainties for parameters such as the b-value or M_{max}. We use the fault

89   network and slip rates taken into account by Nivière et al. (2008), disregarding the Western Rhenish Fault for

90   which, to our knowledge, no slip rate data is available. We assume faults can rupture simultaneously (i.e. multi-

91   segment rupture). In the following sections, we start by describing the concepts and methods we use to constrain

92   the seismogenic potential of the URG, and then describe the data available before discussing the robustness of our

93   results.

94   2   METHOD

95   We use the methodology from Michel et al. (2021) in order to estimate the seismogenic potential of the upper

96   Rhine Graben, including M_{max} and its recurrence time. As in Chartier et al. (2017), we produce seismicity models

97   representative of the long-term behavior of earthquakes. We assume that the MFDs of background earthquakes

98   follow a Gutenberg-Richter power law up to M_{max}. We define background earthquakes as mainshocks, as opposed

99   to their subsequent aftershocks. We assume that their timing of occurrence is random, following a Poisson process.

100   Each model is controlled by three parameters: (1) M_{max}, (2) the recurrence time of events of a certain

101   magnitude, τ_c, and (3) the b-value. We use two types of model, namely the tapered and truncated models (Rollins

102   and Avouac, 2019; Michel et al., 2021; Figure S1). The tapered model type assumes a non-cumulative power-law

103   MFD truncated at M_{max}, which gives rise to a tapered MFD in the cumulative form (i.e. the traditional display

104   when representing the Gutenberg-Richter law). The truncated model type assumes instead a MFD with a

105   distribution truncated at M_{max} in the cumulative form.

106   The seismicity models are then tested against three constraints: (1) the moment budget, as in Chartier et al. (2017),

107   which implies that moment released by slip on the fault should match the moment deficit accumulating between

108   earthquakes over a long period of time; (2) the moment-area scaling law, an empirical scaling law relating rupture

109   area to slip for each earthquake, and (3) the MFD of observed seismicity. Each of these constraints are described

110   in more detail in the following sub-sections. The data and associated uncertainties used for the constraints are

111   discussed in the following section (i.e. Section 3).

112   2.1   Moment budget

113   A moment budget consists in comparing the rate of moment released from slip events (seismic or aseismic),

114    $\dot{m}_0^{Total}$, with the moment deficit rate, $\dot{m}_0^{def}$, accumulating between slip events. The moment deficit rate is defined

115   by the equation $\dot{m}_0^{def} = \int \mu \, \dot{D}^{def} \, dA$, where μ is the shear modulus, A is the area that remains locked during the

116   interseismic period (i.e. the potential seismogenic zone), and $\dot{D}^{def}$ is the rate at which slip deficit builds up. Since

117   the distribution of locked segments of faults and their associated loading rates cannot yet be determined for the

118   URG from geodetic measurements, A is assumed to be homogeneous along-strike for each fault, while we consider

119   possible the seismogenic width to change from one fault to another. The rate at which slip deficit builds up, $\dot{D}^{def}$,

120   is evaluated based on neotectonic information (see Section 3.1). The total moment released, $\dot{m}_0^{Total}$ is calculated

121   based on the rate of moment release of the long-term seismicity model. Since the long-term seismicity model only

122   considers mainshocks, we included a fourth parameter, α_s, that represents the proportion of moment released by

123   background seismicity (Avouac, 2015), m_0^{Bckgrd}, relative to the total moment released (including aftershocks and

124   aseismic afterslip). If $\dot{m}_0^{def} = \dot{m}_0^{Total} = \dot{m}_0^{Bckgrd} / \alpha_s$, then the moment budget is said to be balanced.

125   The cumulative MFD for tapered and truncated seismicity models achieving a balanced moment budget have an

126   analytical form and are a function of M_{max}, b, $\dot{m}_0^{def}$ and α_s (see Rollins and Avouac, 2019, and references therein).

127   We can therefore estimate the probability of a seismicity model balancing the moment budget, P_{Budget}, by

128   sampling the *a priori* distributions of those parameters.

129

2.2   Moment-area scaling law

131   According to global earthquake statistics, the moment released by an earthquake, m_0^{Seis}, is proportional to the area

132   of its rupture, A_{eq}, such that $m_0^{seis} \propto A_{eq}^{3/2}$ (Wells and Coppersmith, 1994; Leonard, 2010; Stirling et al., 2013).

133   We use this scaling to evaluate whether a seismic event of a given magnitude has a rupture area that fits within the

134   seismogenic zone. By considering the spread of the empirical distribution of magnitude vs. area, we assume the

135   probability distribution function of an event of magnitude M_w to be probable considering this scaling, $P_{scaling}$. We

136   use here the self-consistent scaling law, and related uncertainties, as defined by Leonard (2010) in the dip-slip

137   equation (the strike-slip equation is in any case almost the same).

2.3   Earthquake catalog

139   We test whether the observed MFD from earthquake catalogs may be a sample of the distribution of the long-term

140   seismicity models we are building. Effectively, we evaluate the likelihood of our observed MFD given the

141   distribution of the models. Since we only consider mainshocks, we define the likelihood of the observed seismicity

142　catalog, P_{Cat}, as $P_{Cat} = \prod_i P_{poisson}^{M_i}$, where $P_{poisson}^{M_i}$ is the probability to observe $n_{obs}^{M_i}$ events, within the magnitude

143　bin M_i, occurring during the time period $t_{obs}^{M_i}$, assuming the long-term mean recurrence of events is $\tau_{model}^{M_i}$:

144　$P_{poisson}^{M_i}\left(n_{obs}^{M_i}, t_{obs}^{M_i}, \tau_{model}^{M_i}\right) = \dfrac{(t_{obs}^{M_i}/\tau_{model}^{M_i})^{n_{obs}^{M_i}}}{\left(n_{obs}^{M_i}\right)!} e^{-t_{obs}^{M_i}/\tau_{model}^{M_i}}.$

145　Effectively, for a given seismicity model, we generate randomly 2500 declustered earthquake catalogs. We

146　evaluate the likelihood of each catalog and define P_{Cat} as the average of these likelihood values.

147　Note that we follow the recommendation by Felzer (2008) while exploring magnitude uncertainties and correct

148　the magnitudes of each event by $\Delta M = (b^2 \sigma^2)/(2\, log_{10}(e))$, where b is the declustered catalog b-value, σ is the

149　standard deviation for the event's magnitude, and e is the exponential constant.

150　**2.4　Seismicity model probability and marginal probabilities**

151　Finally, the probability of a seismicity model is defined as $P_{SM} = P_{Budget}\, P_{Cat}\, P_{scaling}$ which depends, among

152　others, on M_{max} and b (Michel et al., 2021). The evaluation of the parameters to estimate P_{SM} are discussed in

153　Section 3. Marginal probabilities such as $P_{M_{max}}$, the probability of M_{max}, and P_b, the probability of the b-value,

154　can be estimated based on P_{SM}. We also define $P(\tau_{max}\,|\,M_{max})$ as the probability of the rate of M_{max}, and

155　$P(\tau\,|\,M_w)$ as the probability of the rate of events with magnitude M_w, which accounts for all earthquakes from all

156　of the models (i.e. not only M_{max}). Probabilities needed for estimating seismic hazard (e.g. PSHA) such as the

157　probability to have an event above magnitude M_w for a time period T, $P(M > M_w\,|\,T)$, can likewise be evaluated.

158　**3　DATA AND ASSOCIATED UNCERTAINTIES**

159　We present in this section the data and their associated uncertainties used to evaluate each constraint.

160　**3.1　Neotectonic data, seismogenic along-dip width and moment deficit rate**

161　In order to evaluate the MDR for the moment budget constraint (Section 2.1), we must infer estimates of loading

162　rate (i.e. $\dot{D}^{def}$) for each fault taken into account. The slip rate on each fault is taken from Nivière et al. (2008) for

163　the Rhine River, Black Forest, Weinstetten and Lehen-Schonberg faults (the Landeck or West Renish faults are

164　not considered). Their slip rates rely on estimates of the cumulative vertical displacement of the faults based on

165　Pliocene-Quaternary sediments thickness variations measured from 451 boreholes, assuming that the

166　accommodation space opened by tectonic motion is completely balanced (or over-balanced) by sedimentation.

6

167 However, potential erosional periods due to the piracy of the Rhine River might bias the measurements, thus the

168 values are to be interpreted as maximum displacement estimates. Nivière et al. (2008) inferred vertical slip rates

169 of 0.07 and 0.17 mm/yr from the age of the sediments for the Rhine River and Weinstetten faults respectively. The

170 Lehen-Schonberg fault slip rate reaches between 0.04 and 0.1 mm/yr. While borehole observations do not allow

171 to conclude on the Pliocene-Quaternary slip rate of the Black Forest fault, this structure is suggested to be inactive

172 during this time period, and that the deformation is now accommodated by the other aforementioned faults (Nivière

173 et al., 2008). Note that these are vertical slip rate estimates and the along-strike component is for the moment

174 neglected. For the moment rate calculation, we project vertical slip rates on the along-dip direction considering

175 the dip angles of each fault.

176 The seismogenic down-dip extent of a fault depends on the temperature gradient (e.g. Oleskevich et al., 1999),

177 among other parameters. Indeed, between the isotherms 350°C and 450°C, quartzo-feldspathic rocks undergo a

178 transition in frictional properties (Blanpied et al., 1995) from a rate-weakening (<350°C), potentially seismogenic

179 behavior to a rate-strengthening (>450°C), stable sliding behavior (Dieterich, 1979; Ruina, 1983). The geothermal

180 gradient below the URG is higher than in the surrounding regions due to its tectonic history (Freymark et al.,

181 2017). Based on borehole temperature measurements from Guillou-Frottier et al. (2013), we estimate the envelopes

182 of the geothermal gradient in the southern URG (Figure S2), assuming a linear temperature gradient with depth,

183 and show that the frictional property transition would occur between depths of 6 (shallowest position of the 350°C

184 isotherm; Figure S2) and 18 km (deepest position of the 450°C isotherm; Figure S2). In this study, we define the

185 PDF of the seismogenic down-dip extent as a uniform distribution between 0 and 6 km depth associated with a

186 linear taper down to 18 km. The linearity of the taper implies that the position of the fault's transition to a fully

187 rate-strengthening behavior (>350-450°C) has a uniform probability to fall between 6 km (shallowest position of

188 the 350°C isotherm according to Figure S2) and 18 km depth (deepest position of the 450°C isotherm; Figure S2).

189 Additionally, the southern part of the URG is the site of a potash-salt evaporitic basin (Lutz and Cleintuar, 1999;

190 Hinsken et al., 2007; Freymark et al., 2017), which reaches a maximum depth of ~2 km. Such formations may not

191 accumulate any moment deficit as the yield stress of evaporites is very low (Carter and Hansen, 1983). We assume

192 each fault is potentially impacted by this formation, hence modulating the seismogenic thickness and in turn the

193 seismogenic area available for a rupture. The resulting PDF for the seismogenic thickness is the convolution of

194 the PDF of the down-dip extent of the seismogenic zone with the PDF of the evaporitic basin thickness, giving a

195 uniform distribution between 0 and 2 km. Combining both temperature and salt basin assumptions leads to a PDF

196 of the along-dip seismogenic width, which is uniform down to ~5 km and decreases linearly until ~17 km (Figures

197 S3 to S6).

198 The moment deficit is then the product of the length of each fault, their seismogenic width, the neo-tectonic long-

199 term slip rate, and the shear modulus that we fix to 30 GPa (same as in Chartier et al., 2017). Each fault is assumed

200 to have its own seismogenic width. The moment deficit rate of each fault is shown in Figure 1. The PDFs for each

201 of the fault's constitutive parameters are shown in Figure S3 to S6. By considering the range of the fault's

202 geometrical parameters, which considers also the Black Forest Fault even though it is assumed to be non-active,

203 we obtain the moment-area constraint shown in Figure 2. Events up to $M_w 6.5$ are equiprobable while those

204 above $M_w 7.7$ are extremely improbable.

205 **3.2   Instrumental and historical seismicity catalogs**

206 To constrain the MFD of the long-term seismicity models with an observational seismicity catalog, as described

207 in Section 2.3, we need to evaluate from the observational catalog the number of events per magnitude bin $n_{obs}^{M_i}$

208 over a period of time $t_{obs}^{M_i}$ (Section 2.3). We use the earthquake catalog from Drouet et al. (2020). This catalog was

209 built from multiple former catalogs. It relies mostly on the FCAT-17 catalog (Manchuel et al., 2018), which is

210 itself a combination of the instrumental catalog SiHex (SIsmicité de l'HEXagone; Cara et al., 2015) for the 1965-

211 2009 period, and a historical catalog based on the macroseismic database of SISFRANCE (BRGM, IRSN, EDF),

212 intensity prediction equations from Baumont et al. (2018) and the macroseismic moment magnitude determination

213 from Traversa et al. (2018) for the 463-1965 period. Events located more than 20 km from the French border, not

214 provided by the FCAT-17, are based on the SHEEC catalog (Stucchi et al., 2013; Woessner et al., 2015). Finally,

215 events between2010 and 2016 come from the CEA-LDG bulletins (https://www-dase.cea.fr). All event magnitudes

216 are given in M_w and uncertainties are provided. Anthropic events are expected to be already removed from the

217 catalog (Cara et al., 2015; Manchuel et al., 2018).

218 We select events within the coordinates [6°, 8.5°] longitude and [47°, 49.5°] latitude, i.e. a broad region covering

219 the whole URG, and divide the catalog into two time periods, an instrumental period and a historical one taking

220 events from 1980 onwards and 1850 onwards, respectively. We decluster both catalogs to compare them with the

221 long-term seismicity models (Section 2.3). Declustering is based on the methodology of Marsan et al. (2017),

222 which evaluates the probability that an earthquake is a mainshock. Declustering is applied based on a completeness

223 magnitude, M_c, of 2.2 and 3.2 for the instrumental and historical catalogs, respectively (Text S1; Figures S7 and

224 S8). From the resulting catalogs, we keep events from 1994 onwards and 1860 onwards for the instrumental and

225 historical catalogs, respectively (Figures S7 and S8), in order to avoid border effects from declustering. For the

226 instrumental catalog, 1994 is also the date from which the seismicity rate appears relatively constant (Figure S7).

227 We then select events in the region of interest (i.e. the southern part of the URG), taking into account only

228 earthquakes located within a 10 km buffer around the faults considered, including the Black Forest fault (Figure

229 3). Note that since no events below M_c are considered, there is a lack of events which falls in the magnitude bins

230 directly above M_c while exploring magnitude uncertainties. Thus, when applying the earthquake catalog constraint

231 (Section 2.3), we take events with $M_w \geq 2.8$ and $M_w \geq 4.3$ for the instrumental and historical catalogs,

232 respectively (Felzer, 2008) (Figure 3).

233 **3.3 Constitutive parameters of seismicity models**

234 As mentioned in Section 2.1, the cumulative MFD for tapered and truncated seismicity models balancing the

235 moment budget can be defined as a function of M_{max}, b, $\dot{m}_0^{def}$ and α_s. We explore these parameters using a grid

236 search with M_{max} and b sampled uniformly over $M_{max} \in \mathcal{U}(4.5, 9.9)$ and $b \in \mathcal{U}(0.1, 1.45)$, respectively. Based

237 on global statistics of the post-seismic response following earthquakes (Alwahedi and Hawthorne, 2019; Churchill

238 et al., 2022), we assume that the PDF of α_s is a Gaussian distribution with $\mathcal{N}(0.9, 0.25)$ (Figure S9). Finally, the

239 PDF of the MDR for each fault is assumed to be uniform between 0 and the estimate based on the maximum slip

240 rate from Nivière et al. (2008) (Section 3.1). We thus include scenarios for which almost no moment deficit

241 accumulates on the fault (i.e. the fault slips aseismically or accumulates no strain over long periods of time). This

242 assumption contrasts with the choice made by Chartier et al. (2017) who assume that each fault is fully locked

243 over a seismogenic width terminating at either 15 or 20 km. Doing so, we explore a broad range of possible models.

244 **4 RESULTS**

245 The combination of constraints (Section 2) leads to the results shown in Figure 4. For the truncated model, the

246 marginal probability of P_{SM} in the M_{max} and τ_{max} space is represented by the gray shaded distribution in Figure

247 4 (not shown for the tapered model since the models taper at M_{max}). The marginal probability of M_{max} for the

248 tapered model (in green) peaks at 6.1, while the one for the truncated model (in blue) is bi-modal with peaks at 5.2

249 and 5.8. For the truncated model (not the tapered model for the same reason as previously indicated), the marginal

250 probability $P(\tau_{max} \mid M_{max} = 5.8)$ (solid blue line in the y-axis) peaks at ~1000 yrs. Taking $M_{max} = 6.6$ or 7.0, a

251 number close to the estimated magnitude of the 1356 Basel earthquake, the marginal probability would instead

252 peak at ~16,000 and ~80,000 yrs, respectively.

253   The marginal probabilities $P(\tau \mid M_w = 6.1)$ and $P(\tau \mid M_w = 5.8)$ for the tapered and truncated models (green and

254   blue dotted lines on the y-axis, respectively), which take all events from the seismicity models into account (not

255   only M_{max}), have instead peaks at ~16,000 yrs and ~10,000 yrs, respectively. The marginal probability P_b peaks

256   at ~0.85 and 0.9 for the tapered and truncated models, respectively.

257   The effect with and without the moment-area scaling law is shown in Figure 5. Adding the scaling law constraint

258   does not change the mode of $P_{M_{max}}$ but completely rejects scenarios with M_{max}>7.8.

259   Finally, the probabilities $P(M > M_w \mid T)$ for $T = 100$ and 10,000 yrs are also shown in Figure 5. As an example,

260   the probability of occurrence for an event above $M_w6.5$ (similar to the 1356 Basel earthquake) for an observational

261   period of 100 yrs is ~0.1% for both the tapered and truncated models. For an event above $M_w6.0$ and for the same

262   period, this probability is instead ~1% for both models (see zoom in Figure 5.c).

263   The correlations between M_{max}, the moment deficit rate, the b-value, and α_s, for both the tapered and truncated

264   models but without the scaling law constraint, are shown in Figures S10 and S11. For both models, probable M_{max}

265   increases with increasing b-value (Figure S10.a and S11.a), highlighting strong interdependency between the two

266   parameters. Raising the moment deficit rate will control the minimum probable M_{max} (Figures S10.b and S11.b)

267   but will also tend to exclude scenarios with a high b-value (>1.25; Figures S10.f and S11.f). While other trends

268   are expected between parameters, they seem less visible, likely due to the uncertainties of the parameters explored.

269   The results if we combine the PDFs from the tapered and truncated models using a mixture distribution are shown

270   in Figure S12. $P_{M_{max}}$ has a main peak at 5.9 and a smaller peak at 5.2, which originates from the truncated model.

271    $P(\tau \mid M_w = 5.9)$ peaks instead at ~13 000 yrs.

272   **5   DISCUSSION**

273   **5.1   Sensibility to earthquake catalog declustering**

274   The catalog declustering (i.e. removal of aftershocks) may have a significant impact on the results (Section 2.3),

275   influencing the shape of the observed MFD of earthquakes. In this study, we applied the methodology of Marsan

276   et al. (2017), which is based on the ETAS framework and intrinsically assumes that background events have

277   Poisson behavior. Other declustering methodologies are available and we test here the one from Zaliapin and Ben-

278   Zion (2013) based on the nearest-neighbor distances of events in the space-time-energy domain. The results from

279 this methodology produce background seismicity catalogs with more events than the one from Marsan et al. (2017)

280 (Text S2 and Figures S13 to S15), but infers larger b-values when combining the instrumental catalog with the

281 historical one (as inferred by Figure 6.b). The analysis of the seismogenic potential of the URG using Zaliapin and

282 Ben-Zion (2013) methodology results with $P_{M_{max}}$ peaking at M6.3 for the tapered model, and is still bi-modal for

283 the truncated model, with peaks at M5.2 and M5.9 (Figure 6). Unlike with Marsan et al. (2017), the peak at lower

284 magnitude for the truncated model is more probable than the one at larger magnitude. The most probable M_{max}

285 for both models are slightly shifted to lower magnitudes than the values estimated using Marsan et al. (2017)

286 methodology, but the width of the PDFs appears unchanged to first order. The resulting marginal probabilities

287 $P(\tau \mid M_w = 5.9)$ and $P(\tau \mid M_w = 5.8)$ for the tapered and truncated models both peak at ~8,000 yrs.

288 **5.2   Source of seismicity**

289 We initially selected earthquakes within a 10 km buffer zone around the faults to reflect the spatial strain pattern

290 of a vertical fault blocked down to a depth of 10 km. Nevertheless, the locking depth could potentially be deeper,

291 down to ~18 km as suggested in Section 3.1. In this respect, we also provide results if events are selected within

292 20 km of the faults (Figures S16 and S17). Under these conditions, the seismicity rates of the observational

293 earthquake catalogs are higher and constrain the long-term seismicity models to cases that produce higher moment

294 release rate. $P_{M_{max}}$ thus favours events with a lower magnitude than the one using events within 10 km (Figure 5;

295 Section 4). The tapered model peaks at $M_w 5.9$, instead of 6.1, while the truncated model peaks twice at $M_w 5.2$

296 and 5.8, in a similar manner to the reference scenario in Section 4, except that the peak at $M_w 5.2$ is now the most

297 probable.

298 However, current seismicity in the URG is seemingly diffuse and it is difficult to associate it with a fault in

299 particular (Doubre et al., 2022). On the other hand, geodetic data are not yet able to resolve any tectonic

300 deformation and thus to evaluate the loading rate of faults (Henrion et al., 2020). Even though the Drouet et al.

301 (2020) catalog, based on FCAT-17 catalog, is supposedly devoid of anthropic seismicity (Cara et al., 2015;

302 Manchuel et al., 2018), one can then ask whether the current seismicity is totally representative of the undergoing

303 long-term tectonic processes or presently modulated by surface loads such as the post-glacial rebound (e.g. Craig

304 et al., 2016), aquifer loads, erosion or incision (e.g. Bettinelli et al., 2008; Steer et al., 2014; Craig et al., 2017). If

305 so, the assumption that the main driver of seismicity is tectonic loading breaks down and our method used to assess

306 seismic hazard must be completed by physics-based constraints of such transient stress release (Calais et al., 2016).

307   Distinguishing seismic sources triggered by tectonic loading from other driven forces is an extremely difficult

308   task. The earthquake catalog contribution (Section 2.3) might then not be appropriate.

309   Additionally, the magnitudes of historical events from the FCAT-17 catalog (before the 1960s), and thus the ones

310   from Drouet et al. (2020), seem to be overestimated (or the instrumental events have underestimated magnitudes

311   even though it seems less probable) and a bias of the MFD is thus expected (Beauval and Bard, 2022; Doubre et

312   al., 2022). For the URG case, 3 bins out of 7 of the observed MFD are estimated from the instrumental period. The

313   bins estimated from the historical period have thus slightly more weight in the catalog constraint (Section 2.3).

314   We test an alternative constraint inferring that the possible magnitude and frequency of M_{max} must be consistent

315   with the observed largest event over the observation period (~146 yrs), meaning that it has to be larger than or

316   equal to the known largest event while the return period of the largest event cannot be significantly shorter than

317   the observation period (Approach 2 from Michel et al., 2018). This constraint is equivalent to considering that no

318   earthquakes with a magnitude greater than the largest event in the observation period occurred during the time

319   period covered by the observed catalog. Theoretically, this constraint imposes a lower bound on M_{max} and its

320   recurrence time. The results obtained using this constraint together with the moment budget and scaling law ones

321   are shown in Figure 7. Since M_{max} frequency differs for the tapered and truncated models, the new constraint

322   imposes different lower bounds for the two models. The truncated model rejects scenarios with M_{max} below $M_w 5.5$

323   more strongly. P_b is not constrained by the observed seismicity catalog but higher values of the b-value seem

324   slightly more probable (inset in Figure 7). The marginal probabilities $P(\tau \mid M_w = 5.9)$ and $P(\tau \mid M_w = 6.3)$ for

325   the tapered and truncated models have peaks at ~12,500 yrs and ~63,000 yrs, respectively.

326

327   **5.3   Strike slip component**

328   In this study, as well as in Chartier et al. (2017), we assume solely along-dip displacement since it is the only

329   published neo-tectonic information available. Nevertheless, recent paleo-seismological data on the Black Forest

330   fault near Karlsruhe (north of our study area) suggest 5.9 m of cumulative strike-slip, in contrast to 1.2 m of

331   cumulative vertical slip, over the last 5.9 kyrs (Pena-Castellnou et al., 2023). Those displacements seem to be

332   associated with at least three paleo-earthquakes. This suggests (1) that the Black Forest fault has been active during

333   the Quaternary period and that (2) strike-slip might be predominant. The ratio between strike- and dip-slip from

334   the Black Forest event would be then equal to 4.8. We thus test a scenario where the Black Forest fault is associated

335   with a maximum vertical slip deficit rate of 0.18 mm/yr, as proposed by Jomard et al. (2017), and where we

336   multiply the maximum slip deficit rate of all faults considered by 4.8. The results and the revised MDR for each

337   fault are shown in Figures 8 and S18. $P_{M_{max}}$ peaks at $M_w 6.8$ and $M_w 6.6$ for the tapered and truncated models,

338   respectively. They are associated with the marginal probabilities $P(\tau \mid M_w = 6.8)$ and $P(\tau \mid M_w = 6.6)$ that both

339   peak at ~16,000 yrs for the tapered and truncated models. Note that Pena-Castellnou et al. (2023) suggest that

340   earthquakes of potentially $M_w 6.5$ occurred north of our study area. P_b peaks at 0.7 for both the tapered and

341   truncated models, thus at lower values than taking into account the vertical-slip component alone.

342   The previous scenario tested (Figure 8) takes two more faults (i.e. Weinstetten and Lehen-Schonberg faults) into

343   account than in Chartier et al. (2017), as these two faults are not present within the BDFA (the French database of

344   potentially active faults; Jomard et al., 2017). The results obtained by selecting faults as defined by Chartier et al.

345   (2017) and applying the strike slip assumption are provided in Figure S19. $P_{M_{max}}$ peaks at $M_w 6.7$ and $M_w 6.6$ for

346   the tapered and truncated models, respectively, very similar to the scenario taking all four faults, as the moment

347   deficit rate is dominated by the Rhine River and Black Forest faults. Note that the marginal probabilities $P(\tau \mid M_w)$

348   and $P(\tau_{max} \mid M_{max})$ seem to get more noisy, likely due to the shape of the MDR PDF which skews heavily towards

349   zero (black line in Figure S18.e).

5.4   Multi-segment rupture

351   In this study we assume that all faults can rupture simultaneously. Nevertheless, the Black Forest Fault is initially

352   taken as inactive, and the traces of the Weinstetten and Lehen-Schonberg faults are separated by at least 7.9 km.

353   According to Wesnousky (2006), multi-segment ruptures are associated with low probability when the inter

354   segment distance exceeds 5 km. Consequently, the seismogenic potential scenario from Section 4 would be an

355   overestimation. On the other hand, according to Castellnou et al., 2022, the Black Forest Fault is in fact active and

356   seismogenic, and could be assumed to rupture with other faults. Additional structures might actually link all the

357   faults together (e.g. Lutz and Cleintuar, 1999; Bertrand et al., 2006; Rotstein and Schaming, 2011). In this case,

358   the seismogenic potential scenario from Section 4 would be interpreted as an underestimation.

359   Finally, we only consider the faults within a finite zone, which controls the total seismogenic area of the faults (i.e.

360   the moment-area scaling law effect), whereas the faults continue northwards and southwards to a lesser extent.

361   According to Weng and Yang (2017), the aspect ratio (width to length ratio of a rupture) of dip-slip events barely

362   reaches beyond 8. Taking a seismogenic width of 18 km (our maximum estimate), the maximum length of

363 earthquakes would then be 144 km, while the full length of the URG faults considered, including the Black Forest

364 fault, is ~250 km (~160 km if the Black Forest fault is not included). The rupture of all the faults would then be

365 unlikely. On the other hand, strike-slip events do not seem to be capped by any aspect ratio (Weng and Yang,

366 2017), so M_w>7.5 events cannot be excluded in this context.

367 **6   CONCLUSION**

368 In this study, we investigate the seismogenic potential of the south-eastern URG, building on the work byChartier

369 et al. (2017). Based on a complex fault network (Nivière et al., 2008), we evaluate scenarios that have not been

370 accounted for previously, exploring uncertainties on M_{max}, its recurrence time, the *b*-value, and the moment

371 released aseismically or through aftershocks (see Table 2 for a summary of the results considering the different

372 scenarios). Uncertainties for the MDR, the observed MFD, and the moment-area scaling law are also explored.

373 Given the four faults considered, and the scenario in which the Black Forest fault is no longer active but where the

374 other faults can still rupture simultaneously, the M_{max} maximum probability is estimated at M_w6.1 and M_w5.8

375 using the tapered or the truncated seismicity models respectively. Nevertheless, $P_{M_{max}}$ for the truncated model has

376 a second peak at M_w5.2 and the recurrence time of events of such magnitude (not only M_{max}), $P(\tau \mid M_w = 5.2) \sim$

377 2,000 yrs, is much shorter than the one estimated using the main peak, $P(\tau \mid M_w = 5.8) \sim$ 10,000 yrs. Again

378 considering the scenario excluding the Black Forest fault, there is a 99% probability that M_{max} is less than 7.3

379 using either the tapered or truncated models. In contrast, when strike-slip kinematics are considered as described

380 in Section 5.3 and the Black Forest Fault is taken into account, there is a 99% probability that M_{max} is less than

381 7.6 and 7.5 for the tapered and truncated models, respectively. This is our preferred scenario as it is based on recent

382 findings for strike-slip mechanisms, although the assumptions made in this analysis are debatable (i.e. strike-

383 slip/dip-slip ratio evaluated on a fault just north of our zone of study and applied to all faults; Section 5.3).

384 It should be noted that seismic hazard studies often place an upper bound on the values of M_{max} considered. In

385 the case of the URG, studies that use varying approaches to ours, have yielded values comparable to, or marginally

386 lower than the 99th percentile of $P_{M_{max}}$ of our strike-slip scenario (e.g. M7.4, M 7.1 and M7.5 for Grunthal et al.,

387 2018, Drouet et al., 2020, and Danciu et al., 2021, respectively).

388 In any case, within this study, strong assumptions still had to be made that certainly affected the results. It includes

389 the methodology used to decluster the earthquake catalogs, determining whether it is wise to compare the loading

390 rate of each fault with seismicity, opting to only consider the dip-slip component despite the fact that strike-slip is

391 highly probable, covering the possibility of multi-segment ruptures and even the choice of the faults to be

392 considered. Further work, from paleo-seismology, seismic reflection, geodesy, or earthquake relocation is needed

393 to obtain more information on the structures tectonically involved and their associated loading rates, and to better

394 constrain the URG seismic hazard.

395 **7 CODE AVAILABILITY**

396 **8 DATA AVAILABILITY**

397 **9 AUTHOR CONTRUBUTION**

398 **10 COMPETING STATEMENT**

399 The authors acknowledge there are no conflicts of interest recorded.

400 **11 ACKNOWLEDGEMENT**

404

12 REFERENCES

Alwahedi, M. A., and J. C. Hawthorne, 2019, Intermediate-Magnitude Postseismic Slip Follows Intermediate-Magnitude (M 4 to 5) Earthquakes in California, Geophys. Res. Lett., 46, no. 7, 3676–3687, doi: 10.1029/2018GL081001.

Anderson, J. G., and J. E. Luco, 1983, Consequences of slip rate constraints on earthquake occurrence relations, Bull. - Seismol. Soc. Am., 73, no. 2, 471–496, doi: https://doi.org/10.1785/BSSA0730020471.

Avouac, J.-P., 2015, From Geodetic Imaging of Seismic and Aseismic Fault Slip to Dynamic Modeling of the Seismic Cycle, Annu. Rev. Earth Planet. Sci., 43, doi: 10.1146/annurev-earth-060614-105302.

Baize, S., E. M. Cushing, F. Lemeille, and H. Jomard, 2013, Updated seismotectonic zoning scheme of Metropolitan France, with reference to geologic and seismotectonic data, Bull. la Société Géologique Fr., 184, no. 3, 225–259, doi: 10.2113/gssgfbull.184.3.225.

Barth, A., J. R. R. Ritter, and F. Wenzel, 2015, Spatial variations of earthquake occurrence and coseismic deformation in the Upper Rhine Graben, Central Europe, Tectonophysics, 651–652, 172–185, doi: 10.1016/j.tecto.2015.04.004.

Baumont, D., K. Manchuel, P. Traversa, C. Durouchoux, E. Nayman, and G. Ameri, 2018, Intensity predictive attenuation models calibrated in Mw for metropolitan France, Bull. Earthq. Eng., 16, no. 6, 2285–2310, doi: 10.1007/s10518-018-0344-6.

Beauval, C., and P. Bard, 2022, History of probabilistic seismic hazard assessment studies and seismic zonations in mainland France, Comptes Rendus. Géoscience, 353, no. S1, 413–440, doi: 10.5802/crgeos.95.

Bertrand, G., P. Elsass, G. Wirsing, and A. Luz, 2006, Quaternary faulting in the Upper Rhine Graben revealed by high-resolution multi-channel reflection seismic, Comptes Rendus Geosci., 338, no. 8, 574–580, doi: 10.1016/j.crte.2006.03.012.

Bettinelli, P., J. P. Avouac, M. Flouzat, L. Bollinger, G. Ramillien, S. Rajaure, and S. Sapkota, 2008, Seasonal variations of seismicity and geodetic strain in the Himalaya induced by surface hydrology, Earth Planet. Sci. Lett., 266, nos. 3–4, 332–344, doi: 10.1016/j.epsl.2007.11.021.

Blanpied, M. L., D. A. Lockner, and J. D. Byerlee, 1995, Frictional slip of granite at hydrothermal conditions, J. Geophys. Res. Solid Earth, 100, no. B7, 13045–13064, doi: 10.1029/95JB00862.

Bommer, J. J., and H. Crowley, 2017, The Purpose and Definition of the Minimum Magnitude Limit in PSHA Calculations, Seismol. Res. Lett., 88, no. 4, 1097–1106, doi: 10.1785/0220170015.

Bonjer, K.-P., 1997, Seismicity pattern and style of seismic faulting at the eastern borderfault of the southern Rhine Graben, Tectonophysics, 275, nos. 1–3, 41–69, doi: 10.1016/S0040-1951(97)00015-2.

Calais, E., T. Camelbeeck, S. Stein, M. Liu, and T. J. Craig, 2016, A new paradigm for large earthquakes in stable continental plate interiors, Geophys. Res. Lett., 43, no. 20, 10,621-10,637, doi: 10.1002/2016GL070815.

Cara, M. et al., 2015, SI-Hex: a new catalogue of instrumental seismicity for metropolitan France, Bull. la Société Géologique Fr., 186, no. 1, 3–19, doi: 10.2113/gssgfbull.186.1.3.

Carter, N. L., and F. D. Hansen, 1983, Creep of rocksalt, Tectonophysics, 92, no. 4, 275–333, doi: 10.1016/0040-1951(83)90200-7.

Chartier, T., O. Scotti, C. Clément, H. Jomard, and S. Baize, 2017, Transposing an active fault database into a fault-based seismic hazard assessment for nuclear facilities – Part 2: Impact of fault parameter uncertainties on a site-specific PSHA exercise in the Upper Rhine Graben, eastern France, Nat. Hazards Earth Syst. Sci., 17, no. 9, 1585–1593, doi: 10.5194/nhess-17-1585-2017.

Churchill, R. M., M. J. Werner, J. Biggs, and Å. Fagereng, 2022, Afterslip Moment Scaling and Variability From a Global Compilation of Estimates, J. Geophys. Res. Solid Earth, 127, no. 4, doi: 10.1029/2021JB023897.

449 Craig, T. J., E. Calais, L. Fleitout, L. Bollinger, and O. Scotti, 2016, Evidence for the release of long-term
450   tectonic strain stored in continental interiors through intraplate earthquakes, Geophys. Res. Lett., 43, no.
451   13, 6826–6836, doi: 10.1002/2016GL069359.

452 Craig, T. J., K. Chanard, and E. Calais, 2017, Hydrologically-driven crustal stresses and seismicity in the New
453   Madrid Seismic Zone, Nat. Commun., 8, no. 1, 2143, doi: 10.1038/s41467-017-01696-w.

454 Danciu, L. et al., 2021, The 2020 update of the European Seismic Hazard Model: Model Overview.
455   https://doi.org/10.3929/ethz-b-000590386

456 Dieterich, J. H., 1979, Modeling of Rock Friction Experimental Results and Constitutive Equations, J. Geophys.
457   Res., 84, no. B5, 2161–2168, https://doi.org/10.1029/JB084iB05p02161

458 Doubre, C., M. Meghraoui, F. Masson, S. Lambotte, H. Jund, M. Bès de Berc, and M. Grunberg, 2022,
459   Seismotectonics in Northeastern France and neighboring regions, Comptes Rendus. Géoscience, 353, no.
460   S1, 153–185, doi: 10.5802/crgeos.80.

461 Drouet, S., G. Ameri, K. Le Dortz, R. Secanell, and G. Senfaute, 2020, A probabilistic seismic hazard map for
462   the metropolitan France, Bull. Earthq. Eng., 18, no. 5, 1865–1898, doi: 10.1007/s10518-020-00790-7.

463 Fäh, D. et al., 2009, The 1356 Basel earthquake: an interdisciplinary revision, Geophys. J. Int., 178, no. 1, 351–
464   374, doi: 10.1111/j.1365-246X.2009.04130.x.

465 Felzer, K. R., 2008, Calculating California seismicity rates, Tech. Rep., Geological Survey (US),
466   https://doi.org/10.3133/ofr20071437I

467 Freymark, J., J. Sippel, M. Scheck-Wenderoth, K. Bär, M. Stiller, J.-G. Fritsche, and M. Kracht, 2017, The deep
468   thermal field of the Upper Rhine Graben, Tectonophysics, 694, 114–129, doi: 10.1016/j.tecto.2016.11.013.

469 Fuhrmann, T., M. Caro Cuenca, A. Knöpfler, F. J. van Leijen, M. Mayer, M. Westerhaus, R. F. Hanssen, and B.
470   Heck, 2015, Estimation of small surface displacements in the Upper Rhine Graben area from a combined
471   analysis of PS-InSAR, levelling and GNSS data, Geophys. J. Int., 203, no. 1, 614–631, doi:
472   10.1093/gji/ggv328.

473 Grünthal, G., D. Stromeyer, C. Bosse, F. Cotton, and D. Bindi, 2018, The probabilistic seismic hazard
474   assessment of Germany—version 2016, considering the range of epistemic uncertainties and aleatory
475   variability, Bull. Earthq. Eng., 16, no. 10, 4339–4395, doi: 10.1007/s10518-018-0315-y.

476 Guillou-Frottier, L., C. Carré, B. Bourgine, V. Bouchot, and A. Genter, 2013, Structure of hydrothermal
477   convection in the Upper Rhine Graben as inferred from corrected temperature data and basin-scale
478   numerical models, J. Volcanol. Geotherm. Res., 256, 29–49, doi: 10.1016/j.jvolgeores.2013.02.008.

479 Heidbach, O. et al., 2018, The World Stress Map database release 2016: Crustal stress pattern across scales,
480   Tectonophysics, 744, 484–498, doi: 10.1016/j.tecto.2018.07.007.

481 Heidbach, O., M. Rajabi, K. Reiter, M. O. Ziegler, and WSM Team, 2016, World Stress Map Database Release
482   2016, V. 1.1. GFZ Data Services. https://doi.org/10.5880/WSM.2016.001

483 Henrion, E., F. Masson, C. Doubre, P. Ulrich, and M. Meghraoui, 2020, Present-day deformation in the Upper
484   Rhine Graben from GNSS data, Geophys. J. Int., 223, no. 1, 599–611, doi: 10.1093/gji/ggaa320.

485 Hinsken, S., K. Ustaszewski, and A. Wetzel, 2007, Graben width controlling syn-rift sedimentation: the
486   Palaeogene southern Upper Rhine Graben as an example, Int. J. Earth Sci., 96, no. 6, 979–1002, doi:
487   10.1007/s00531-006-0162-y.

488 Jomard, H., E. M. Cushing, L. Palumbo, S. Baize, C. David, and T. Chartier, 2017, Transposing an active fault
489   database into a seismic hazard fault model for nuclear facilities – Part 1: Building a database of potentially
490   active faults (BDFA) for metropolitan France, Nat. Hazards Earth Syst. Sci., 17, no. 9, 1573–1584, doi:
491   10.5194/nhess-17-1573-2017.

492 Kraft, T., and N. Deichmann, 2014, High-precision relocation and focal mechanism of the injection-induced
493   seismicity at the Basel EGS, Geothermics, 52, 59–73, doi: 10.1016/j.geothermics.2014.05.014.

494 Leonard, M., 2010, Earthquake Fault Scaling: Self-Consistent Relating of Rupture Length, Width, Average
495   Displacement, and Moment Release, Bull. Seismol. Soc. Am., 100, no. 5A, 1971–1988, doi:
496   10.1785/0120090189.

497 Lutz, M., and M. Cleintuar, 1999, Geological results of a hydrocarbon exploration campaign in the southern
498   Upper Rhine Graben (Alsace Centrale, France), Bull. für Angew. Geol., 4, 3–80, doi:
499   http://doi.org/10.5169/seals-221515.

500 Manchuel, K., P. Traversa, D. Baumont, M. Cara, E. Nayman, and C. Durouchoux, 2018, The French seismic
501   CATalogue (FCAT-17), Bull. Earthq. Eng., 16, no. 6, 2227–2251, doi: 10.1007/s10518-017-0236-1.

502 Marsan, D., M. Bouchon, B. Gardonio, H. Perfettini, A. Socquet, and B. Enescu, 2017, Change in seismicity
503   along the Japan trench, 1990-2011, and its relationship with seismic coupling, J. Geophys. Res. Solid
504   Earth, 122, no. 6, 4645–4659, doi: 10.1002/2016JB013715.

505 Mayer-Rosa, D., and B. Cadiot, 1979, A review of the 1356 Basel earthquake: Basic data, Tectonophysics, 53,
506   nos. 3–4, 325–333, doi: 10.1016/0040-1951(79)90077-5.

507 Mazzotti, S. et al., 2021, FMHex20: An earthquake focal mechanism database for seismotectonic analyses in
508   metropolitan France and bordering regions, BSGF - Earth Sci. Bull., 192, 10, doi: 10.1051/bsgf/2020049.

509 Michel, S., J. Avouac, R. Jolivet, and L. Wang, 2018, Seismic and Aseismic Moment Budget and Implication for
510   the Seismic Potential of the Parkfield Segment of the San Andreas Fault, Bull. Seismol. Soc. Am., 108, no.
511   1, 19–38, doi: 10.1785/0120160290.

512 Michel, S., R. Jolivet, C. Rollins, J. Jara, and L. Dal Zilio, 2021, Seismogenic Potential of the Main Himalayan
513   Thrust Constrained by Coupling Segmentation and Earthquake Scaling, Geophys. Res. Lett., 48, no. 13, 1–
514   10, doi: 10.1029/2021GL093106.

515 Molnar, P., 1979, Earthquake Recurrence Intervals and Plate Tectonics, 115–133.
516   https://doi.org/10.1785/BSSA0690010115

517 Nivière, B., A. Bruestle, G. Bertrand, S. Carretier, J. Behrmann, and J.-C. Gourry, 2008, Active tectonics of the
518   southeastern Upper Rhine Graben, Freiburg area (Germany), Quat. Sci. Rev., 27, nos. 5–6, 541–555, doi:
519   10.1016/j.quascirev.2007.11.018.

520 Oleskevich, D. A., R. D. Hyndman, and K. Wang, 1999, The updip and downdip limits to great subduction
521   earthquakes: Thermal and structural models of Cascadia, south Alaska, SW Japan, and Chile, J. Geophys.
522   Res. Solid Earth, 104, no. B7, 14965–14991, doi: 10.1029/1999JB900060.

523 Pena-Castellnou, S. et al., 2023, First evidence of surface rupturing earthquakes in the eastern Rhine Graben
524   Boundary Fault (Germany). https://dx.doi.org/10.2139/ssrn.4472340

525 Rollins, C., and J. Avouac, 2019, A Geodesy- and Seismicity-Based Local Earthquake Likelihood Model for
526   Central Los Angeles, Geophys. Res. Lett., 46, no. 6, 3153–3162, doi: 10.1029/2018GL080868.

527 Rotstein, Y., and M. Schaming, 2011, The Upper Rhine Graben (URG) revisited: Miocene transtension and
528   transpression account for the observed first-order structures, Tectonics, 30, no. 3, doi:
529   10.1029/2010TC002767.

530 Rouland, D., H. Haessler, K. P. Bonjer, B. Gilg, D. Mayer-Rosa, and N. Pavoni, 1983, The Sierentz Southern-
531   Rhinegraben Earthquake of July 15, 1980. Preliminary Results, in *Developments in Solid Earth*
532   *Geophysics*, 441–446,doi: 10.1016/B978-0-444-99662-6.50086-1

533 Ruina, A., 1983, Slip instability and state variable friction laws, J. Geophys. Res. Solid Earth, 88, no. B12,
534   10359–10370, doi: 10.1029/JB088iB12p10359.

535 Steer, P., M. Simoes, R. Cattin, and J. B. H. Shyu, 2014, Erosion influences the seismicity of active thrust faults,
536   Nat. Commun., 5, no. 1, 5564, doi: 10.1038/ncomms6564.

537 Stirling, M., T. Goded, K. Berryman, and N. Litchfield, 2013, Selection of Earthquake Scaling Relationships for
538   Seismic-Hazard Analysis, Bull. Seismol. Soc. Am., 103, no. 6, 2993–3011, doi: 10.1785/0120130052.

539   Stucchi, M. et al., 2013, The SHARE European Earthquake Catalogue (SHEEC) 1000–1899, J. Seismol., 17, no.
540   2, 523–544, doi: 10.1007/s10950-012-9335-2.

541   Traversa, P., D. Baumont, K. Manchuel, E. Nayman, and C. Durouchoux, 2018, Exploration tree approach to
542   estimate historical earthquakes Mw and depth, test cases from the French past seismicity, Bull. Earthq.
543   Eng., 16, no. 6, 2169–2193, doi: 10.1007/s10518-017-0178-7.

544   Wells, D. L., and K. J. Coppersmith, 1994, New empirical relationships among magnitude, rupture length,
545   rupture width, rupture area, and surface displacement, Bull. Seismol. Soc. Am., 84, no. 4, 974–1002, doi:
546   https://doi.org/10.1785/BSSA0840040974.

547   Weng, H., and H. Yang, 2017, Seismogenic width controls aspect ratios of earthquake ruptures, Geophys. Res.
548   Lett., 44, no. 6, 2725–2732, doi: 10.1002/2016GL072168.

549   Wesnousky, S. G., 2006, Predicting the endpoints of earthquake ruptures, Nature, 444, no. 7117, 358–360, doi:
550   10.1038/nature05275.

551   Woessner, J. et al., 2015, The 2013 European Seismic Hazard Model: key components and results, Bull. Earthq.
552   Eng., 13, no. 12, 3553–3596, doi: 10.1007/s10518-015-9795-1.

553   Zaliapin, I., and Y. Ben-Zion, 2013, Earthquake clusters in southern California I: Identification and stability, J.
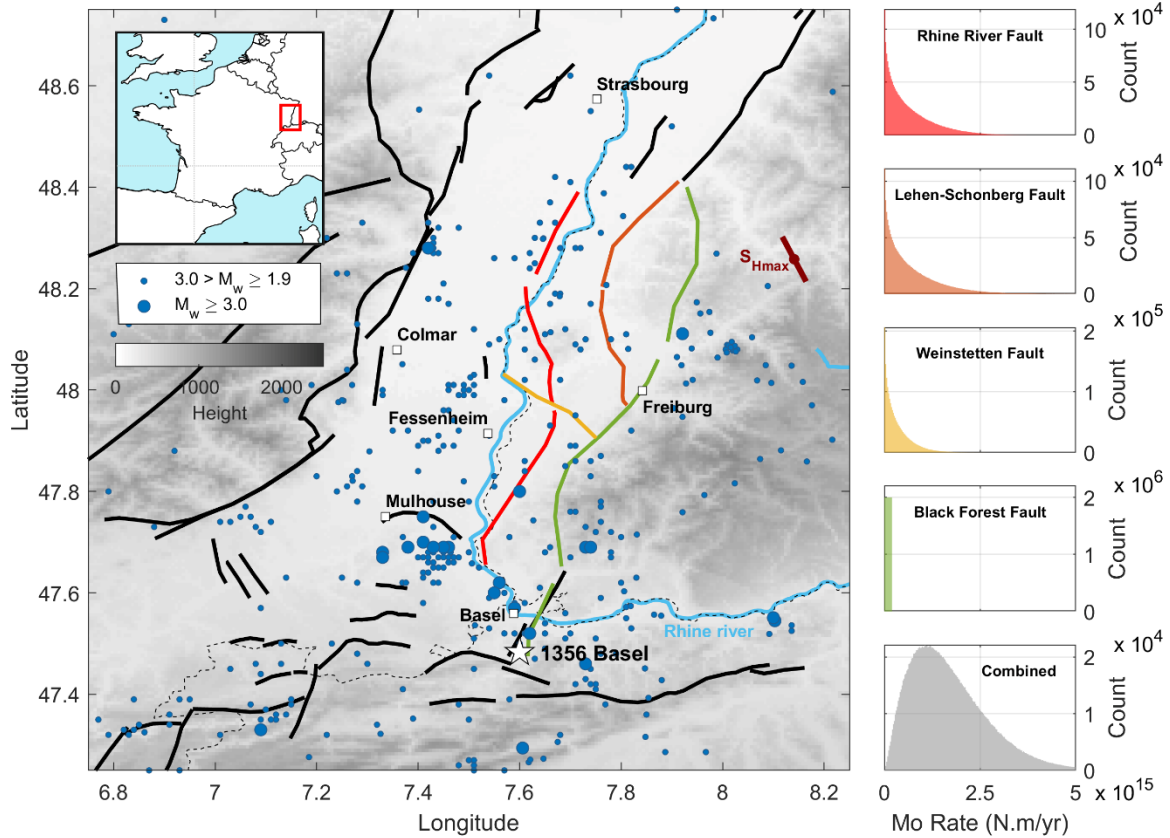554   Geophys. Res. Solid Earth, 118, no. 6, 2847–2864, doi: 10.1002/jgrb.50179.

555

556

557

558

559

560

Figure 1: (Left panel) Regional setting and seismicity of the Upper Rhine Graben (Drouet et al., 2020). Black lines are faults while colored ones are the faults taken into account in this study. The fault network geometry is based on the BDFA database (Jomard et al., 2017) and Nivière et al. (2008). Blue dots are epicenters of $M_w > 2.2$ earthquakes since 1994. The white star indicates the 1356 Basel earthquake (magnitude ranging from M6.5+/-0.5 (Manchuel et al., 2017) to M6.9+/-0.2 (Fäh et al., 2009)). The brown bar indicates the approximate orientation of the maximum horizontal compressional stress (S_{Hmax}) (Heidbach et al., 2016, 2018). The thin dashed black line is the border between France and Germany. The nuclear powerplant of Fessenheim and the main cities are indicated by white squares. (Right panels) Moment deficit rate PDFs (expressed in counts) for each of the four faults considered (colors are indicative of the faults in the left panel), and their combination (in grey).

570
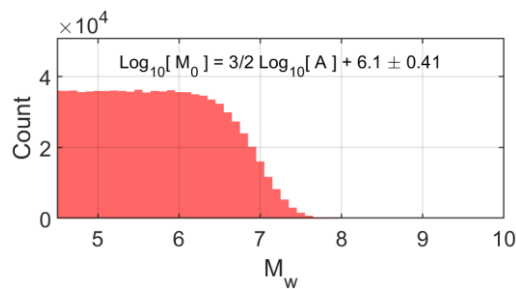
Figure 2: PDF of M_w considering the along-dip moment-area scaling law of earthquakes from Leonard (2010). Note that the area from the Black Forest Fault is not included, as its loading rate is assumed equal to 0 mm/yr.

20
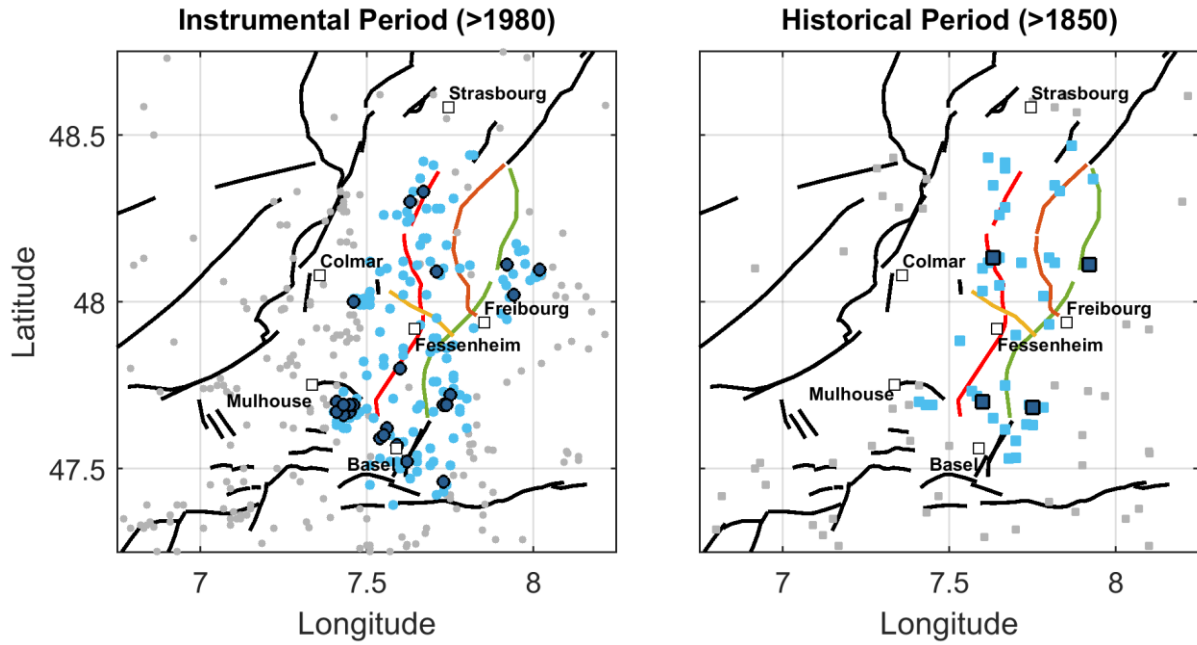
**Figure 3: Earthquake selection for the instrumental (>1994) and historical (>1850) periods. Gray dots and squares indicate all earthquakes with $M_c = 2.2$ and 3.2 for the instrumental and historical catalogs, respectively. Light blue dots and squares indicate earthquakes taken into account for the seismogenic potential analysis. Dark blue dots and squares indicate $M_w \geq 2.8$ and 4.3 earthquakes taken into account for the seismogenic potential analysis.**

580
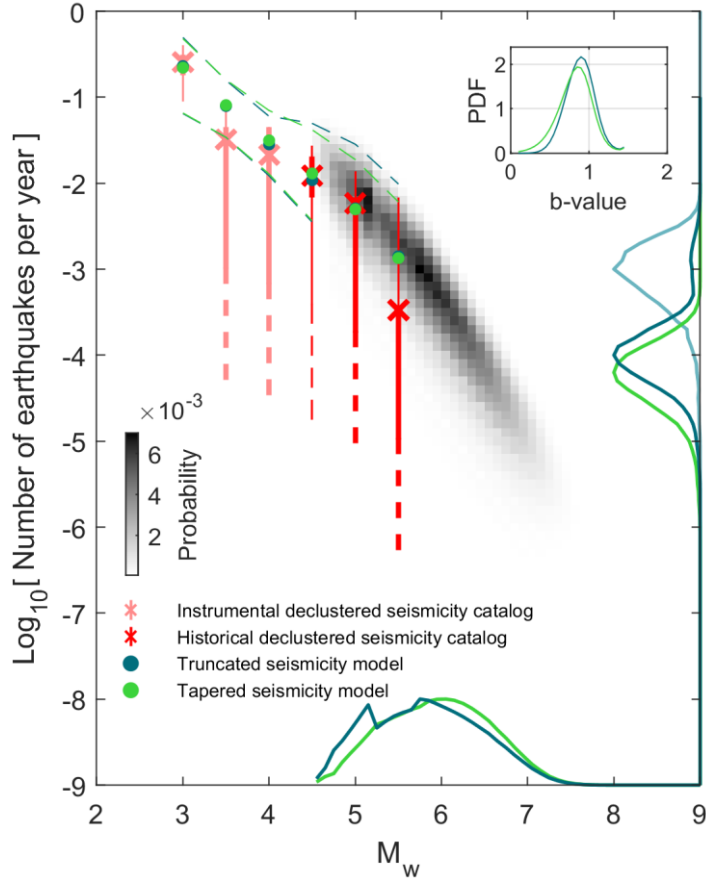
Figure 4: Seismogenic potential of the URG using all constraints: moment budget, observed magnitude-frequency distribution, and moment area scaling law. The rate of occurrence of historical and instrumental earthquakes, within their observation periods, are indicated by red and pink crosses and error bars, respectively. Thick and thin error bars indicate the 15.9-84.1% (1-sigma) and 2.3-97.7% (2-sigma) quantiles of the MFDs. Dashed lines show the spread of possible MFDs for the 2500 catalogs randomly generated to explore uncertainties. The green and blue colors are associated with the tapered and truncated long-term seismicity models. Green and blue dots show the means of the marginal PDF for the long-term seismicity. Dashed green and blue lines indicate the spread of the best 1% seismicity models. The marginal probabilities of M_{max}, $P_{M_{max}}$, are indicated by the solid lines on the M_w axis. They have been normalized so that their amplitude is equal to one instead of 0.60 and 0.59 for the tapered and truncated models, respectively. Green and dark blue lines on the earthquake frequency axis indicate the probability of the rate of events, τ, with magnitude $M_w = M_{Mode}$, thus $P(\tau \mid M_w = M_{Mode})$, with M_{Mode}=6.1 and 5.8 for the tapered and truncated models, respectively, considering all magnitudes in the seismicity models and not only the recurrence rate of M_{max}. They have also been normalized and their peaks were initially at 1.13 and 1.17 for the tapered and truncated models, respectively. The light blue line on the earthquake frequency axis indicates $P(\tau_{max} \mid M_{max} = 5.8)$ (for the truncated seismicity model only) and is normalized so that its amplitude equals one instead of 1.19. The top-right inset shows the marginal probability of the b-value. Note that the seismicity MFDs shown in the figure are not in the cumulative form.

597
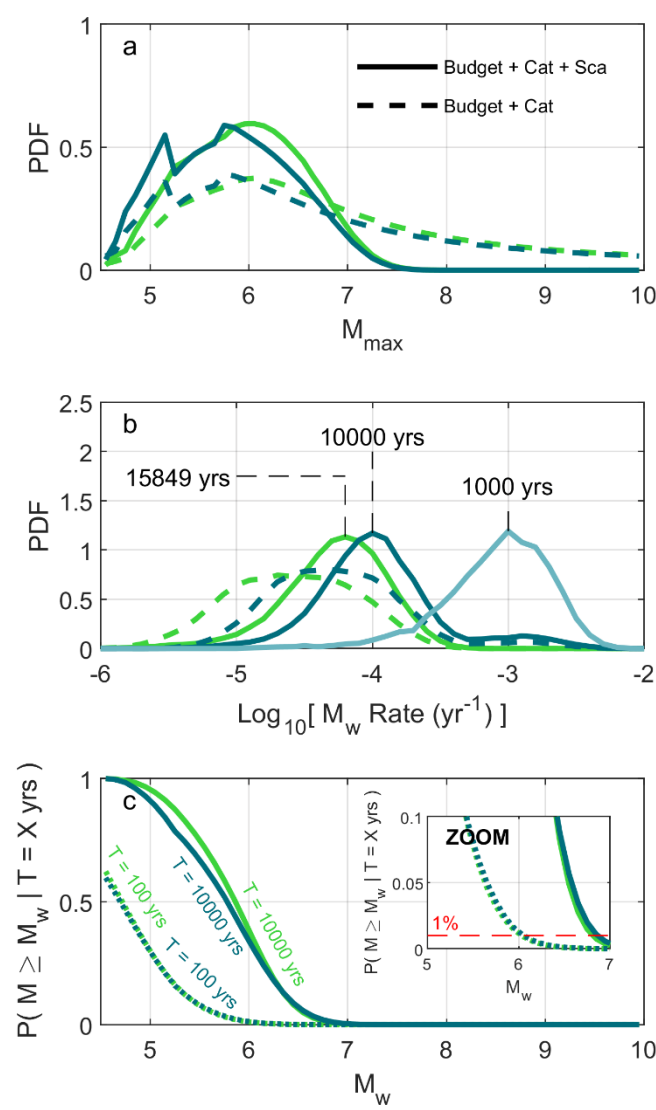
Figure 5: (a) Evolution of the marginal PDF of M_{max} when adding the moment-area scaling law constraint. The green and blue colors in the figure are associated with the tapered and truncated long-term seismicity models. (b) Same as (a) but for the marginal PDF of the recurrence time of events: $P(\tau \mid M_w = 6.1)$ and $P(\tau \mid M_w = 5.8)$ for the tapered and truncated models (dark blue and green lines), respectively, and $P(\tau_{max} \mid M_{max} = 5.8)$ shown only for the truncated model (solid light blue line). (c) Probability of occurrence of earthquakes with a magnitude larger than M_w over a period of X yrs. We show the probability of occurrence of such events for the 100 yrs and 10,000 yrs time periods. In (a), (b) and (c), dotted lines represent the marginal PDFs considering both the moment budget and seismicity catalog constraint, the dashed lines indicate the PDFs when the earthquake scaling constraint is added. The inset in (c) is a zoom of the panel. The 1% probability of exceedance over a time period of 100 yrs is a typical order of magnitude for nuclear applications in France.

608
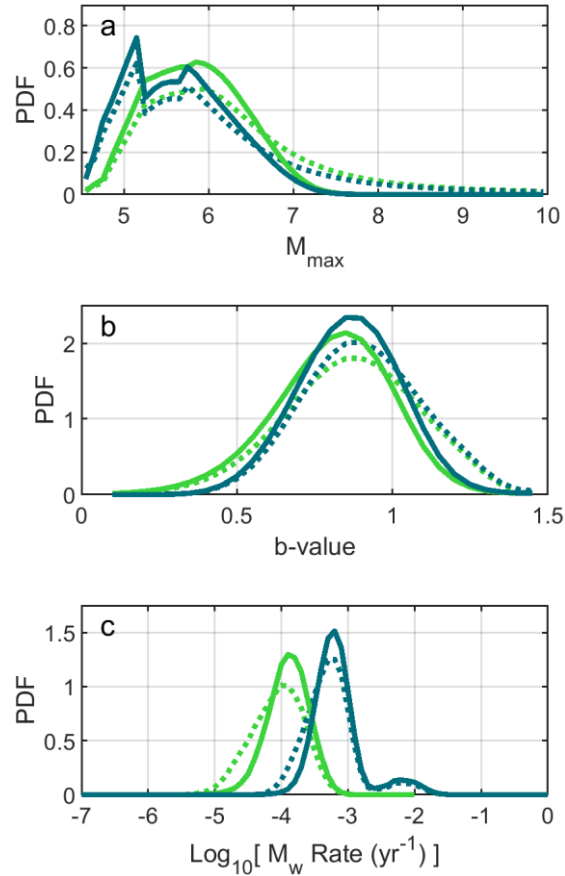
Figure 6: Results using the declustering method from Zaliapin and Ben-Zion (2013) instead of Marsan et al. (2017) (Text S2). In this scenario, no probabilities of events to be mainshocks are defined. (a) M_{max} PDF. (b) b-value PDF. (c) $P(\tau \,|\, M_w = M_{Mode})$ PDF. Solid lines correspond to the results using all constraints while the dotted lines only use the moment budget and earthquake catalog constraints. Green and blue lines correspond to the tapered and truncated models, respectively. The results shown here are the ones taking a b-value equal to 1 for Zaliapin and Ben-Zion (2013) declustering method. The results for b-values of 0.5 and 1.5 are also shown in Figure S15 and are relatively similar to the ones obtained using a b-value of 1.0.
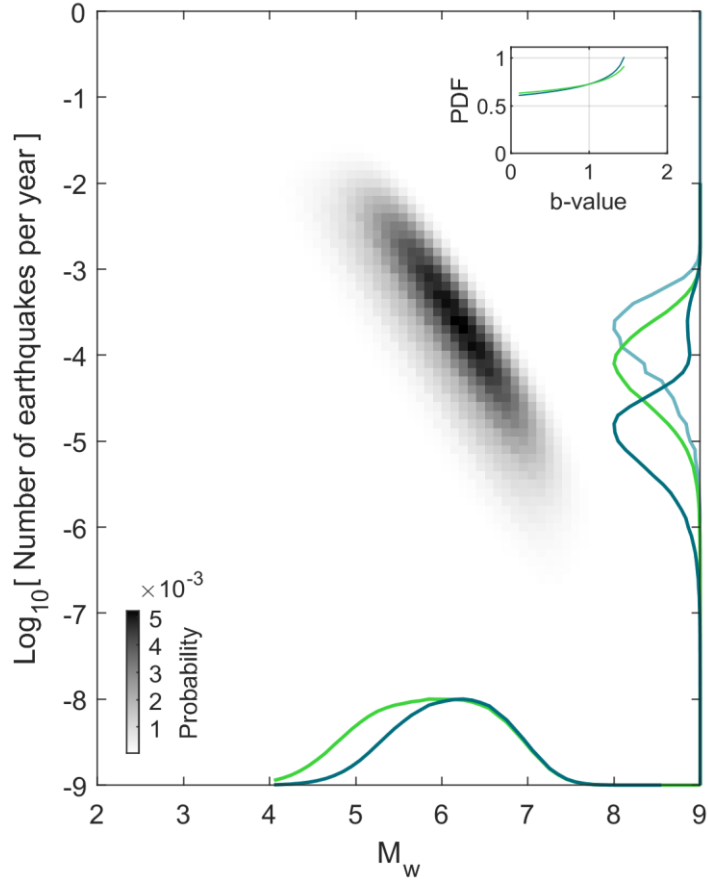
Figure 7: Same as Figure 4 but only considering the constraints for the moment budget, the moment-area scaling law, and the one on M_{max} frequency considering the time period of the catalog (which serves as a lower bound constraint for M_{max}; Section 5.2; Approach 2 from Michel et al., 2018). The marginal probabilities $P_{M_{max}}$ have been normalized so that their amplitude is equal to one instead of 0.46 and 0.58 for the tapered and truncated models, respectively. The same is true for $P(\tau \mid M_w = M_{Mode})$ which were initially of 0.85 and 0.81 of amplitude, and $P(\tau_{max} \mid M_{max} = 6.3)$ (for the truncated seismicity model only) which peaked at an amplitude of 0.85.
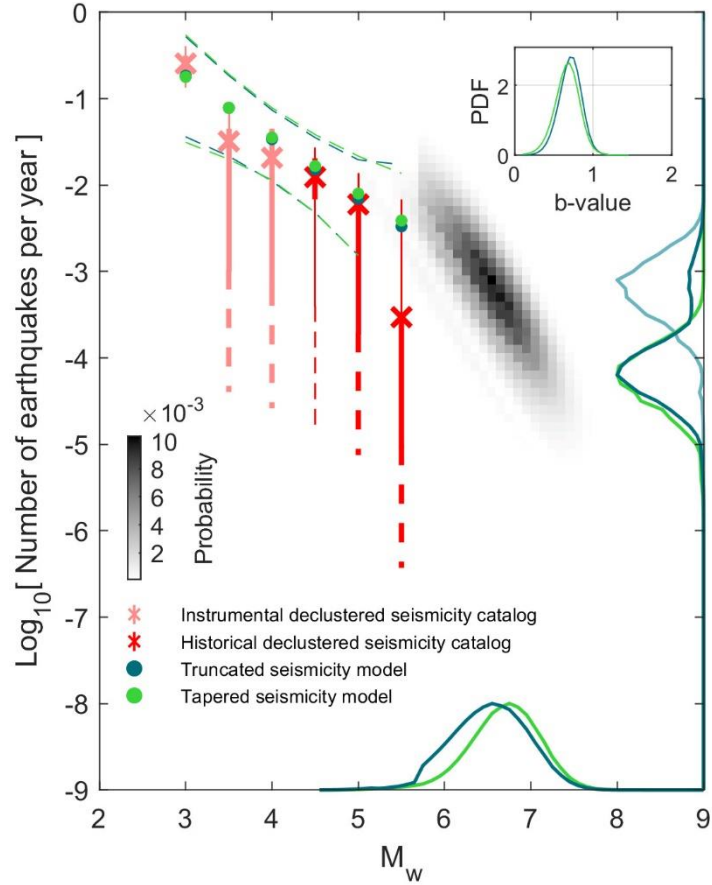
Figure 8: Same as Figure 2 but considering a strike-slip slip rate component equivalent to 4.8 times the dip-slip estimate, and assuming the Black Forest Fault maximum long-term vertical slip rate is 0.18 mm/yr (as proposed by Jomard et al., 2017). Leonard et al.'s (2010) strike-slip moment-area scaling law is used here for the scaling law constraint, even though it is very similar to the dip-slip version. The marginal probabilities $P_{M_{max}}$ have been normalized so that their amplitude is equal to one instead of 1.02 and 0.88 for the tapered and truncated models respectively. The same is truefor $P(\tau \mid M_w = M_{Mode})$ which were initially of 1.15 and 1.13 of amplitude, and $P(\tau_{max} \mid M_{max} = 6.6)$ (for the truncated seismicity model only) which peaked at an amplitude of 1.17.

632 **Table 1: Fault parameters. $\mathcal{U}$ and $\mathcal{N}$ stands for uniform and normal distribution. The PDFs of each of these parameters**

633 **and the resulting moment deficit rate for each fault are shown in Figure S3 to S6.**

Fault Name	Segment Name (from BDFA)	Dip (°)	Length (km)	Slip-Rate (mm/yr)	Seismogenic zone down-dip extent (km)	Evaporite layer thickness (km)
Rhine River Fault	FRR-1	$\mathcal{U}(50,80)$	$\mathcal{N}(35,2)$	$\mathcal{U}(0,0.07)$	(1) Uniform from 0 to 6 km in depth. (2) Linearly decreasing from 6 to 18 km depth. Does not apply to the Black Forest Fault as its loading rate is assumed equal to 0 mm/yr	$\mathcal{U}(0,2)$
Rhine River Fault	FRR-2	$\mathcal{U}(50,80)$	$\mathcal{N}(25,2)$	$\mathcal{U}(0,0.07)$		$\mathcal{U}(0,2)$
Rhine River Fault	FRR-3	$\mathcal{U}(55,85)$	$\mathcal{N}(20,2)$	$\mathcal{U}(0,0.07)$		$\mathcal{U}(0,2)$
Black Forest Fault	FFN-1	$\mathcal{U}(35,75)$	$\mathcal{N}(20,5)$	0		$\mathcal{U}(0,2)$
Black Forest Fault	FFN-2	$\mathcal{U}(40,80)$	$\mathcal{N}(50,2)$	0		$\mathcal{U}(0,2)$
Black Forest Fault	FFN-3	$\mathcal{U}(35,75)$	$\mathcal{N}(35,2)$	0		$\mathcal{U}(0,2)$
Lehen-Schonberg		$\mathcal{U}(40,80)$	$\mathcal{N}(54,2)$	$\mathcal{U}(0,0.1)$		$\mathcal{U}(0,2)$
Weinstetten		$\mathcal{U}(40,80)$	$\mathcal{N}(15,2)$	$\mathcal{U}(0,0.17)$		$\mathcal{U}(0,2)$

634

635

636

637 **Table 2: Summary of the results considering the different scenarios tested from section 4 to 5.3.**

Scenarios	Modes of M_{max}	99% probability that M_{max} is below magnitude M_w	Mode of $P(\tau \mid M_w = M_{Mode})$
Rhine River Fault + Lehen-Schonberg Fault + Weinstetten Fault *Dip-Slip Only Marsan et al. (2017) Declus.* (Section 4 / Fig. 4 and 5)	Tapered Model M_w 6.1 Truncated Model M_w 5.2 and 5.8	Tapered Model M_w 7.3 Truncated Model M_w 7.3	Tapered Model τ =16,000 yrs Truncated Model τ = 2,000 and 10,000 yrs
Rhine River Fault + Lehen-Schonberg Fault + Weinstetten Fault *Dip-Slip Only Zaliapin and Ben-Zion (2013) Declus.* (Section 5.1 / Fig. 6)	Tapered Model M_w 5.9 Truncated Model M_w 5.2 and 5.8	Tapered Model M_w 7.2 Truncated Model M_w 7.1	Tapered Model τ =8,000 yrs Truncated Model τ = 1,600 and 8,000 yrs
Rhine River Fault + Lehen-Schonberg Fault + Weinstetten Fault *Dip-Slip Only Marsan et al. (2017) Declus. Loose catalog constraint (Approach 2 from Michel et al., 2018)* (Section 5.2 / Fig. 7)	Tapered Model M_w 5.9 Truncated Model M_w 6.3	Tapered Model M_w 7.4 Truncated Model M_w 7.4	Tapered Model τ =12,500 yrs Truncated Model τ = 63,000 yrs
Rhine River Fault + Lehen-Schonberg Fault + Weinstetten Fault + Black Forest Fault *Strike- and Dip-Slip Marsan et al. (2017) Declus.* (Section 5.3 / Fig. 8)	Tapered Model M_w 6.8 Truncated Model M_w 6.6	Tapered Model M_w 7.6 Truncated Model M_w 7.5	Tapered Model τ =16,000 yrs Truncated Model τ = 16,000 yrs

638

639